Received: 16 November 2023 | Revised: 31 March 2024 | Accepted: 26 April 2024

DOI: 10.1002/qj.4760

Quarterly Journal of the Royal Meteorological Society

RESEARCH ARTICLE

Dynamic channel selection based on vertical sensitivities for the assimilation of FY-4A geostationary interferometric infrared sounder targeted observations

Yonghui Li[1,2] | **Wei Han**[3] | **Wansuo Duan**[1,2]

[1]State Key Laboratory of Numerical Modeling for Atmospheric Sciences and Geophysical Fluid Dynamics, Institute of Atmospheric Physics, Chinese Academy of Sciences, Beijing, China

[2]University of Chinese Academy of Sciences, Beijing, China

[3]CMA Earth System Modeling and Prediction Centre (CEMC), China Meteorological Administration, Beijing, China

Correspondence
Wei Han, CMA Earth System Modeling and Prediction Centre (CEMC), China Meteorological Administration, Beijing, 100081, China.
Email: hanwei@cma.gov.cn

Wansuo Duan, State Key Laboratory of Numerical Modeling for Atmospheric Sciences and Geophysical Fluid Dynamics, Institute of Atmospheric Physics, Chinese Academy of Sciences, Beijing, 100029, China.
Email: duanws@lasg.iap.ac.cn

Funding information
National Key Research and Development Program of China, Grant/Award Number: 2022YFC3004004; International Partnership Program of Chinese Academy of Sciences, Grant/Award Number: 060GJHZ2022061MI; National Natural Science Foundation of China, Grant/Award Number: 42075155

Abstract

Target observations have garnered significant attention owing to their successful applications in enhancing forecasting skills of extreme weather events, particularly tropical cyclone (TC) events. The key step of implementing target observation is to determine the sensitive area in advance. Previous studies often obtained the sensitive areas for TC forecasting by vertically integrating the energy of optimal perturbation and taking the horizontal area of large energy, in an attempt to use it to represent roughly the sensitivity of the whole atmospheric layer. The advent of the geostationary interferometric infrared sounder on the FY-4A satellite and then corresponding satellite data assimilation have opened up a new possibility for identifying the vertical sensitivity for TC forecasting to improve the forecasting skill. This article proposes a targeting satellite channel (TSC) approach to accurately capture the sensitivity along vertical directions of the atmosphere that allows one to preferentially select the channels whose observations locate on the sensitive vertical atmospheric layers. Numerical experiments demonstrate that, when preferentially assimilating the channel observations obtained from the TSC approach, the TC tracks achieve a considerably smaller forecast error than the information entropy channel selection approach. The TSC approach, therefore, has the potential for the satellite data assimilation to improve TC track forecasting skill very effectively, which can also provide guidance to targeting observations in field campaigns for TC forecasting.

KEYWORDS

channel selection, FY-4A GIIRS, targeted observation

1 | INTRODUCTION

Studies on predictability (Froude *et al.*, 2007; Rabier *et al.*, 1996; Reynolds *et al.*, 1994; Simmons & Hollingsworth, 2002) have revealed that a significant portion of forecast errors typically stem from uncertainties in the initial field. Therefore, obtaining an accurate estimation of the initial field presents an effective approach to enhance forecasting skills of numerical weather prediction (Simmons, 1995). Targeted observation, also known as adaptive observation (Snyder, 1996), is recognized as an effective observation strategy that improves the accuracy of the initial field, which aims at enhancing forecasting skills by strategically adding additional observations in sensitive areas where the initial error grows rapidly and leads to significant forecast errors. It has been employed in various field observation experiments, such as The Fronts and Atlantic Storm-Track Experiment (Joly *et al.*, 1997), the North Pacific Experiment (Langland *et al.*, 1999), and the Dropsonde Observations for Typhoon Surveillance near the Taiwan Region (Chun Chieh *et al.*, 2005, 2007). Recently, several field experiments focusing on targeted observations of typhoons have been conducted (Feng *et al.*, 2022; Qin *et al.*, 2023). The outcomes of these observation experiments consistently demonstrate that, on average, targeted observations contribute to improved forecasting skills (Bergot, 1999; Bergot *et al.*, 1999; Feng *et al.*, 2022; Qin *et al.*, 2023).

There have been a lot of studies on targeting or targeted observations for extreme weather events forecasting, particularly tropical cyclones (TCs). In these previous studies, the sensitive areas for targeting observation were generally determined by vertically integrating energy to obtain a two-dimensional field, with the large-value areas regarded as the sensitive areas (Majumdar *et al.*, 2002; Qin & Mu, 2014; Torn, 2014; Zhou & Mu, 2011a). That is to say, the vertical atmospheric layers covered by the horizontal sensitive areas are all roughly thought of as being sensitive to extreme weather events forecasting. Presently, the geostationary interferometric infrared sounder (GIIRS) carried by the FY-4A Fengyun geostationary weather satellite (Di *et al.*, 2018; Menzel *et al.*, 2018; Yang *et al.*, 2017) has become a popular observing device, especially for the forecasts of high-impact weather events such as typhoons. This instrument provides large-scale, continuous, fast, and precise data, significantly enhancing weather forecasting skills (Yin *et al.*, 2021). The spectral range of GIIRS spans from 700 to 1,130 cm^{-1} (8.85–14.29 μm) and from 1,650 to 2,250 cm^{-1} (4.44–6.06 μm) with the same spectral interval of 0.625 cm^{-1}. Figure 1 illustrates the brightness temperature values obtained from the 1,650 channels of GIIRS, which capture valuable information about the various layers of the atmosphere. When evaluating the sensitivity of forecasts to initial errors, it becomes necessary to assess the vertical sensitivity of sensitive regions while assimilating FY-4A GIIRS satellite data. This allows for the precise selection of highly effective channels, thereby significantly enhancing forecasting skills for specific weather events. However, the aforementioned horizontal sensitive areas cannot describe exactly the vertical sensitivity of the atmospheric layers, and the error at the specific atmospheric layers with high vertical sensitivity will significantly affect the evolution of weather events. Therefore, it is necessary to recognize the vertical sensitivity of the atmosphere. This would help optimize the selection of the channel of GIIRS hyperspectral data and eliminate data redundancy and observation correlations while maximizing the provision of observation information and finally providing a much more economic assimilation strategy.

At present, one of the most widely used channel selection methods is derived from the theory of Rodgers (1998), which describes an iterative method to determine an optimal set of channels based on their information content—hereafter called the information entropy (IE) method. The effectiveness of the IE method has been proven (Collard, 2007; Coopmann *et al.*, 2020; Rabier *et al.*, 2002; Yin *et al.*, 2019). The principle of the IE method is based on the understanding that positions with a larger background field error correspond to higher uncertainty. The channels selected by the IE method aim to minimize the uncertainty of background error covariance. This leads to a significant reduction in background field errors at these positions after assimilating these channels. However, the observations from these channels may not necessarily help reduce the errors, which has the potential to result in significant forecast errors in the future, and these channels may not present the observations at the atmospheric layers with high vertical sensitivity for the weather events forecasting of concern.

In this study, inspired by the target observing theorem, we propose a new satellite channel selection method for GIIRS to select the most sensitive observation channel for forecast errors. For convenience, we call this method the "targeting satellite channel" (TSC) approach (see Section 2 for details). The TSC cares about the sensitivity of the forecast on initial errors along the vertical direction, and then is able to provide the channel observations that have the greatest potential to lower forecast errors. The effectiveness of this method will be verified by typhoon track forecasting in this study.

The structure of this article is as follows. Section 2 provides an introduction to the TSC method employed in the study. Section 3 describes the experimental design, including details about the model, observational data, and specific cases used in the analysis. The results obtained from the experiments are presented in Section 4 and are summarized and discussed in Section 5.

2 | STRATEGY OF CHANNEL SELECTION

The channel selection method proposed in this article is based on the IE method. We will introduce the IE method in Section 2.1, and the channel selection method TSC proposed in this article is presented in Section 2.2.

2.1 | Information entropy

When Shannon created information theory in 1949, he found a unique quantity to measure the uncertainty of information sources called IE, also known as Shannon entropy (Shannon, 1949). A large number of scholars have applied this method to the channel selection of hyperspectral infrared detection data (Collard, 2007;

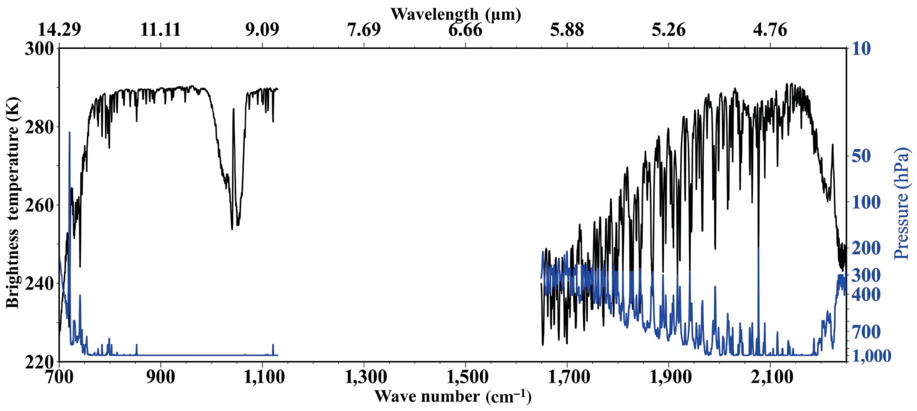

FIGURE 1 The brightness temperatures value (black line) and weighting function peak layer (blue line) of the FY-4A GIIRS' 1,650 channels, which obtain infrared radiance in long-wave infrared and middle-wave infrared that respectively cover the spectral ranges of 700–1,130 cm^{-1} (8.85–14.29 μm) with a spectral interval of 0.625 cm^{-1} and 1,650–2,250 cm^{-1} (4.44–6.06 μm) with the same spectral interval. [Colour figure can be viewed at wileyonlinelibrary.com]

Rabier *et al.*, 2002; Rodgers, 1998; Yin *et al.*, 2019). The following is a brief introduction to the IE method; see Collard (2007) for details. If the probability distribution of the system before and after assimilating the observation is respectively $P_1(x)$ and $P_2(x)$, then the information capacity of the observation can be defined as the difference H between the IE of the two states:.

$$H = S(P_1) - S(P_2), \tag{1}$$

where $S(P_1)$ and $S(P_2)$ are the IE of the system before and after data assimilation. In data assimilation theory, it is commonly assumed that the probability distribution of systematic errors follows a Gaussian distribution. Then, the IE of the systematic error can be represented as follows:

$$S(P) = \frac{1}{2} \ln |M|, \tag{2}$$

where M is the covariance matrix of the systematic error. If the error covariance matrix of the current background field is recorded as B and the error covariance matrix after assimilating observation is A, then the information capacity H contained in the observation process can be expressed as

$$H = \frac{1}{2} \ln |B| - \frac{1}{2} \ln |A|. \tag{3}$$

A is recorded as the analysis error covariance matrix, which can be obtained through the assimilation formula:

$$A = B - BH^{\mathrm{T}}(HBH + R)^{-1}HB. \tag{4}$$

The IE method involves iterating through the available channels. The steps for channel selection are as follows:

1. Calculate the information capacity H for each channel using Equation (3). Select the channel with the maximum H value at this iteration.
2. Update the error covariance matrix B by replacing it with the error covariance matrix A calculated in the previous step. Exclude the channels that have been selected in the previous iterations and select a channel corresponding to the maximum H in the remaining set of channels.
3. Repeat steps 1 and 2 until a sufficient number of channels have been selected or H no longer changes significantly.

By iterating through the channels and selecting the one with the maximum information capacity at each step, the method ensures that the channels with the most informative capacity are chosen.

2.2 | Targeting satellite channel

To identify the specific initial errors that lead to large forecast errors in the future, the initial step of the TSC method involves estimating vertical sensitivity and recognizing the sensitive atmospheric layers (for convenience, hereafter termed vertical sensitive areas; see Appendix A for details) by calculating optimal initial perturbations and horizontally integrating the perturbation energy—see Equation (A.3). For the sake of facilitating subsequent comparisons, the perturbation energy within these vertical sensitive areas is standardized and denoted as the sensitive area index (SA). Then, the background error covariance was constructed according to the vertical sensitivity. The specific reconfiguration practices are as follows. When calculating the background error covariance in the vertical direction, it is necessary to calculate the background error standard deviation in different layers. This background error standard deviation is multiplied by the sensitive area index to obtain a weighted background error covariance matrix, denoted as B'. The formula for constructing matrix B' is as follows:

$$\sigma'(z_i) = \sigma(z_i) \times \mathrm{SA}_i, \quad i = 1, \ldots, n, \tag{5}$$

$$B'(z_i, z_j) = \sigma'(z_i) \times \sigma'(z_j) \times \rho(z_i, z_j), \quad i, j = 1, \ldots, n, \tag{6}$$

where $\sigma(z_i)$ is the background error standard deviation at height z_i, $\sigma'(z_i)$ is the background error standard deviation after weighting at height z_i, n is the maximum layer of height, SA_i is the sensitive area index at layer i, $\rho(z_i, z_j)$ is the error correlation coefficient between layer i and layer j, and $B'(z_i, z_j)$ is the background error covariance after weighting between layer i and layer j. It is emphasized here that B' is an $n \times n$ matrix, which is the background error covariance in the vertical direction. The next steps are the same as for the IE method (see Section 2.1 for details). By iterating through the channels and selecting the one with the maximum information content at each step, the TSC ensures that the channels with the most informative content of high vertical sensitivity areas are chosen. This iterative process allows for an effective selection of channels based on their information content, leading to a relatively optimal set of channels for data assimilation.

IE, one of the most widely used channel selection methods, differs from TSC only in that it does not modify B. From the two methods mentioned herein, it can be inferred that the TSC method modifies B before executing the IE method. IE establishes the maximum information content as the selection criterion, with the aim of maximizing the reduction of the overall errors in the vertical direction of the initial field. This essentially entails minimizing errors in areas with large background errors; see Equation (3). However, it is known that larger background errors do not necessarily lead to larger forecast errors. Small errors in sensitive areas can also result in significant forecast errors. This is where the TSC method, introduced in this article, plays a crucial role. TSC revises the background error covariance matrix using the sensitive area index, weighting errors more heavily within sensitive areas; see Equation (5). The revised B will have larger errors in sensitive areas. Subsequently, the same procedure as in the IE method is employed to select channels. Then, the TSC method focuses more on reducing the initial errors that would lead to significant forecast errors than the IE method.

It is important to highlight that this article focuses primarily on the temperature channel of the GIIRS, with a specific focus on the background error covariance matrix associated with temperature variables. Therefore, when referring to the background error covariance matrix in the following, we refer to the temperature background error covariance matrix.

3 | EXPERIMENTAL SET-UP

To validate the rationality and effectiveness of TSC, a series of assimilation and forecasting experiments are designed using six typhoon cases. These experiments aimed to assess the performance of the proposed method in improving the initial field and subsequent forecast accuracy for typhoon events.

3.1 | The model

We use the China Meteorological Administration (CMA) global forecast system (GFS) in this study. The CMA-GFS consists of 87 vertical layers, with the highest layer at 0.1 hPa, and it covers the entire global area with a horizontal resolution of 25 km (0.25° × 0.25°). The model employs a C grid for the horizontal grid and a Charney–Phillips grid for the vertical grid. It utilizes hybrid coordinates for the vertical coordinate system and employs a fully compressible non-hydrostatic model core with a semi-implicit and semi-Lagrangian discretization scheme.

In terms of physics parametrizations, the CMA-GFS employs various schemes. For example, it uses the Rapid Radiative Transfer Model for general circulation models long-wave (V4.71)/short-wave (V3.61) scheme to improve the effective radius of ice clouds (Morcrette *et al.*, 2008; Pincus *et al.*, 2003). It also employs the new simplified Arakawa–Schubert scheme, the CMA self-developed dual-parameter microphysics scheme and large-scale cloud condensation scheme, the CMA self-developed explicit cloud cover forecasting scheme (Ma *et al.*, 2018), the new Mellor-Yamada-Rumtsev-Fairall (NMRF) boundary layer parameterization scheme based on a Charney–Phillips grid (Chen *et al.*, 2020), and the Common Land Model scheme to optimize the latent heat flux calculation process (Dai *et al.*, 2003). Furthermore, it includes the gravity-wave drag scheme based on Kim and Arakawa (1995) and the Lott and Miller (1997) approach.

Another very important component is the CMA-GFS four-dimensional variational assimilation system. Designed for operational application, this assimilation system utilizes an incremental analysis method and is divided into outer and inner iterations (Zhang *et al.*, 2019). To reduce computational burden, the outer circulation of the assimilation employs a nonlinear model with a horizontal resolution of 0.25°, whereas the tangent linear and adjoint models in the inner circulation have a horizontal resolution of 1°. Moreover, simplified physical processes are applied during the inner circulation.

3.2 | Cases

Since the detection range of the FY-4A GIIRS is the East Asia region (3° N–55° N, 66° E–144° E), we have selected six typhoon cases from the western Pacific for our study: *Chan-hom* and *Maysak* in 2020 and *Conson* and *Chanthu*

TABLE 1 Basic information about typhoons studied.

Typhoon	Case no.	Duration	Maximum intensity and time	Analysis time	Forecast length (days)
Maysak	1	0000 UTC Aug 28–1800 UTC Sep 3, 2020	52 m·s^{-1}, 940 hPa, 0600 UTC Sep 1	0600 UTC Aug 31, 2020	4
	2			0600 UTC Sep 1, 2020	4
Chan-hom	3	1800 UTC Oct 3–1200 UTC Oct 12, 2020	38 m·s^{-1}, 965 hPa, 0000 UTC Oct 9	0600 UTC Oct 8, 2020	4
Conson	4	0600 UTC Sep 6–1800 UTC Sep 15, 2021	30 m·s^{-1}, 982 hPa, 0600 UTC Sep 8	1200 UTC Sep 9, 2021	4
Chanthu	5	0000 UTC Sep 7–1800 UTC Sep 17, 2021	68 m·s^{-1}, 905 hPa, 1200 UTC Sep 10	1200 UTC Sep 8, 2021	4
	6			0600 UTC Sep 13, 2021	4

in 2021, which caused severe impacts on East Asia. Table 1 provides detailed information about these typhoon cases, including their lifetimes, intensities, and other relevant details. Notably, case 6 exhibits an abnormal track (see the black line of Figure 9f), which allows us to assess the effectiveness of the TSC method in forecasting typhoons with an abnormal track.

3.3 | The design of experiments

In this research, the vertical sensitive areas are determined by the leading singular vector (LSV) method (see Appendix A for details), which is widely utilized in operational forecasting centers such as European Centre for Medium-Range Weather Forecasts (Yamaguchi & Majumdar, 2010), the Japan Meteorological Agency (Yamaguchi *et al.*, 2009), and the CMA (Wang *et al.*, 2020). This method allows us to identify areas in the vertical domain that have a significant impact on forecast accuracy. Owing to linearity of the LSV, it is important to consider the optimization time for targeted observations. If the optimization time is too long, the nonlinearity of the system will become significant and may impact the effectiveness of the sensitive areas of LSV; thus, the optimization time selected here is 24 hr (Zhou & Mu, 2012a). For the selection of the verification area, Zhou and Mu (2011b) suggested that the verification areas should include the typhoon location at verification time. Therefore, for each typhoon case, the verification area is chosen as the area where the typhoon is projected to reach at the verification time.

Before applying the IE method or TSC for channel selection, it is necessary to preprocess the channels and establish a blacklist to eliminate channels with large observation noise or poor simulation. In this research, a threshold of 0.15 K (at 300 K) for the noise-equivalent delta temperature is used to select channels for the

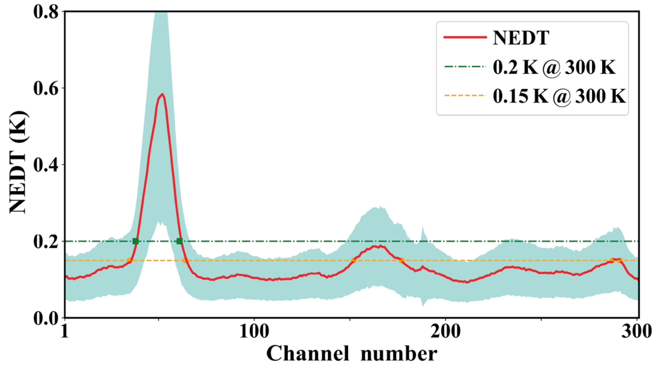

FIGURE 2 Noise-equivalent delta temperature (NEDT) corresponding to the first 300 channels of the geostationary interferometric infrared sounder (red line). The blue region represents the corresponding standard deviation, the orange dotted line is the 0.15 K (at 300 K) threshold, and the green dotted line is the 0.2 K (at 300 K) threshold. [Colour figure can be viewed at wileyonlinelibrary.com]

blacklist (Figure 2). In this study, 56 channels are selected for the blacklist, with larger noise-equivalent delta temperature values mainly concentrated between channels 35 and 65 (721.875–740.625 cm^{-1}). This article pays attention to the part of the long-wave channels of the GIIRS; specifically, channels 1–300 (700-887.5 cm^{-1}). These channels primarily capture temperature information related to the sensitive areas of interest.

To evaluate the impact of assimilating radiation data from the different channels of the FY-4A GIIRS on typhoon analysis and forecasting, we design three experiments for each typhoon case. In the first experiment, the baseline experiment, denoted "No_GIIRS", CMA-GFS does not assimilate the observation of the GIIRS and other observations. In the second experiment experiment, the control experiment, denoted "EXP_CTRL", CMA-GFS only assimilates the observation of the GIIRS within the 6-hr time window. The channels used for assimilation in this experiment are selected by the IE method, and the remaining observations are not assimilated. In the third experiment, named "EXP_SEN", a similar assimilation process is conducted as in EXP_CTRL but the channels are selected by the TSC method (see Table 2 for details). The design of these three experiments serves two purposes: first, to demonstrate the effectiveness of the GIIRS data by comparing the No_GIIRS experiment with the latter two; and second, to compare EXP_SEN with EXP_CTRL, highlighting the differences between channel selection by the TSC and IE methods, and analyzing their respective impacts on typhoon forecasting, thereby underscoring the role of sensitive areas.

Free forecasting is performed with an output frequency of 6 hr. The best track dataset to verify the typhoon track forecast comes from the CMA Tropical Cyclone Data Center (Xiaoqin *et al*., 2021; Ying *et al*., 2014) (for the source of the dataset, please log in to https://tcdata.typhoon.org.cn). Considering the calculation efficiency, observation error correlation and entropy reduction H (amount of information), here we select the first 60 channels for both EXP_CTRL and EXP_SEN. The sum of entropy reduction H associated with these channels accounts for approximately 76% of the total entropy reduction H (Figure 3b) for EXP_CTRL. This indicates that by selecting only one-fifth of the channels we are able to explain a significant portion of the assimilation increment. It is worth noting that the channels selected by the IE method for different cases are consistent in EXP_CTRL. Similarly, for EXP_SEN, we selected the top 60 channels identified by the TSC method. In addition, the sum of entropy reduction H is shown in Supporting Information Figure S1 for each individual case.

4 | RESULTS

4.1 | Selected channels

The difference between the TSC and IE methods lies in the modification of the background error covariance in TSC, which increases the initial uncertainty of the position with a large sensitive area index and concentrates the observation information in the sensitive areas of interest.

Figure 3a illustrates the initial temperature background error covariance of the IE method, which is calculated using the National Meteorological Center method (Parrish & Derber, 1992). It shows that the temperature background error is relatively uniformly distributed at all levels. Consequently, according to the IE theory, the channels selected should be spread throughout the atmosphere. However, in the TSC method the background

TABLE 2 Description of the experimental set-up.

Experiment	Model resolution	Domain	Observations assimilated
EXP_SEN	0.2° × 0.25°	Global Forecast System global analysis	FY-4A GIIRS (channels selected by TSC)
EXP_CTRL	0.25° × 0.25°	Global Forecast System global analysis	FY-4A GIIRS (channels selected by IE)
No_GIIRS	0.25° × 0.25°	Global Forecast System global analysis	Without FY-4A GIIRS

Abbreviations: GIIRS, geostationary interferometric infrared sounder; IE, information entropy; TSC, targeting satellite channel.

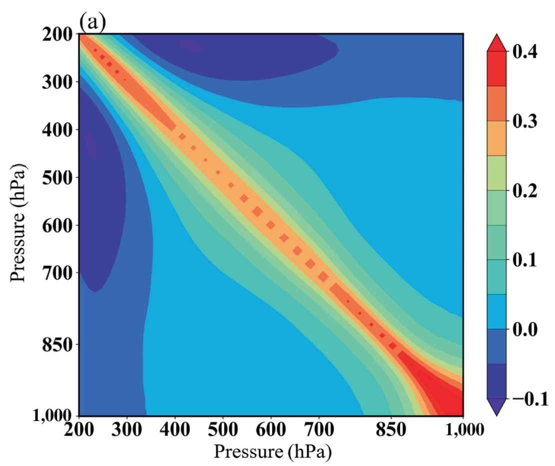

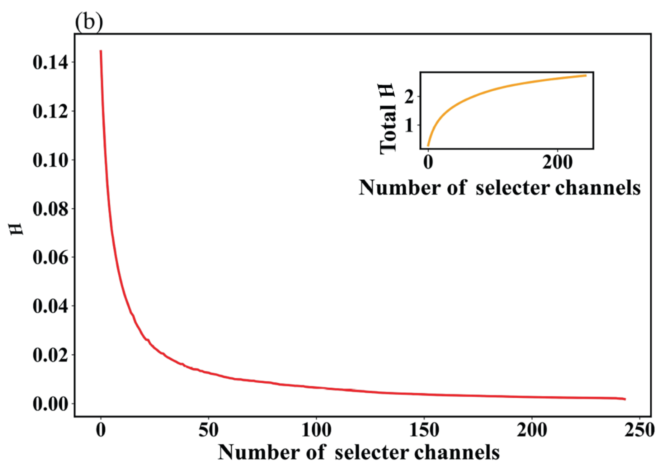

FIGURE 3 (a) The initial background error covariance. (b) Entropy reduction H (red curve) and total entropy reduction H (orange curve) of information entropy. [Colour figure can be viewed at wileyonlinelibrary.com]

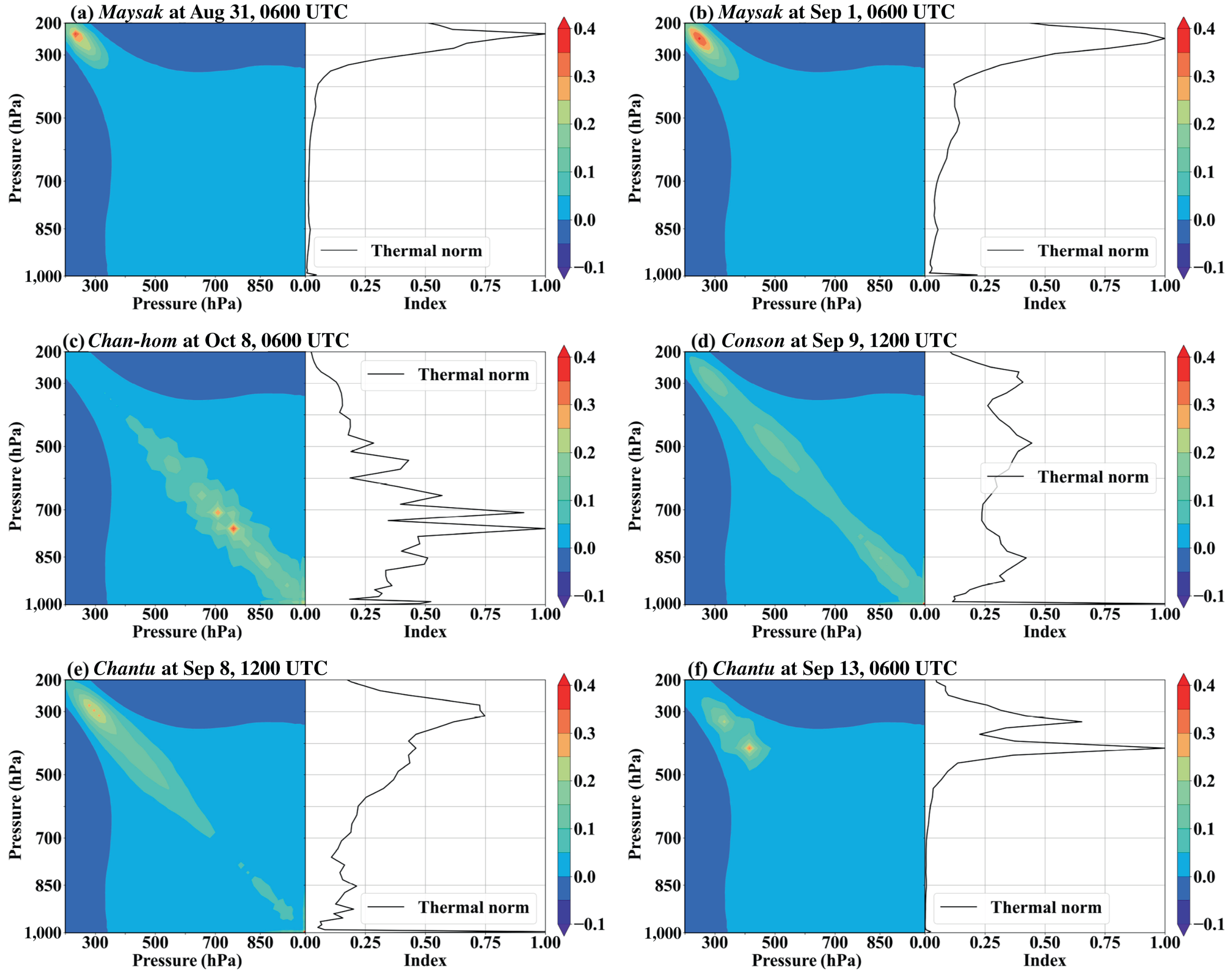

FIGURE 4 Reconstructed background error covariance after weighting (left side of each figure) and sensitive area index (right side of each figure): (a)–(f) Case nos. 1–6 respectively. [Colour figure can be viewed at wileyonlinelibrary.com]

error covariance is weighted by the sensitive area index, resulting in a covariance structure that corresponds to the sensitive areas (Figure 4a–f). For instance, the position of Typhoon *Maysak* (Figure 4a,b) with large sensitive area index is mainly located in the upper troposphere and a small part is located in the lower troposphere, which corresponds to a large background error covariance value in the upper and lower layers. The channels selected theoretically focus on decreasing temperature error in the upper and lower layers; though the sensitive area index of Typhoon *Chan-hom*(Figure 4c) is located in the middle and lower troposphere, the channels selected theoretically focus on decreasing temperature error in the lower and middle layers. It is important to note that the sensitive areas and background error covariance differ for each case. For example, in Figure 4f the *Chanthu* case displays the sensitive areas with distinct double peaks, and the corresponding background error covariance reflects these two prominent areas of large values.

It is well known that the presence of a high-level warm core is a crucial indicator of typhoon formation. TCs, whether in the western Pacific or the northwest Atlantic, typically exhibit warm cores in their upper layers. The development of disturbances within a typhoon is closely linked to the strength of its warm core structure. In other words, the structure of growth-type disturbances in sensitive areas should be closely associated with the warm core. Here, we present the warm core structures of six individual cases (Supporting Information Figure S2). Cases 1, 2, 5, and 6 are severe typhoons or above, and their warm cores are situated in the upper atmosphere, whereas cases 3 and 4 are typhoons or below, locating in the middle and low atmosphere or not obvious. It is evident that the positions of the large-value areas in the sensitive areas correspond to the warm core. For example, the large sensitive area index of cases 1, 2, and 6 are located at the high level, corresponding to the warm core. The large sensitive area index of case 3 is about 800 hPa in the lower atmosphere, which also has a good corresponding relationship with the warm core. Therefore, the channels selected can provide effective observation information for those areas that affect typhoon forecasting.

Figure 5 shows the channels selected by the IE method and the channels selected by the TSC method for the six typhoon cases, which is in line with the aforementioned conclusions. The channels selected by the IE method are distributed across the lower, middle, and upper troposphere (Figure 5a). In the case of EXP_SEN for *Maysak*, the channels are concentrated in the upper and lower troposphere (Figure 5b,c), whereas for EXP_SEN of *Chan-hom* the channels primarily concentrate in the lower troposphere (Figure 5d). For the case of *Chanthu* (Figure 5g), there is a distinct aggregation within the mid-layer and upper layer channels, corresponding to the sensitive areas with distinct double peaks. The channels selected by the TSC method for the remaining two cases are also distributed in the position where the index of the sensitive areas is large (Figure 5e,f).

In addition, we also conduct a Fourier transform on the background error covariances and their respective sensitive area indexes to examine whether they capture information of different scales within the vertical sensitive areas. The results indicate that the sensitive areas of all six cases primarily exhibit low-frequency signals (Figure 6). However, the *Chan-hom* case shows stronger high-frequency signals than the others (the orange line in Figure 6). Kindly note that, in this context, “large scale”

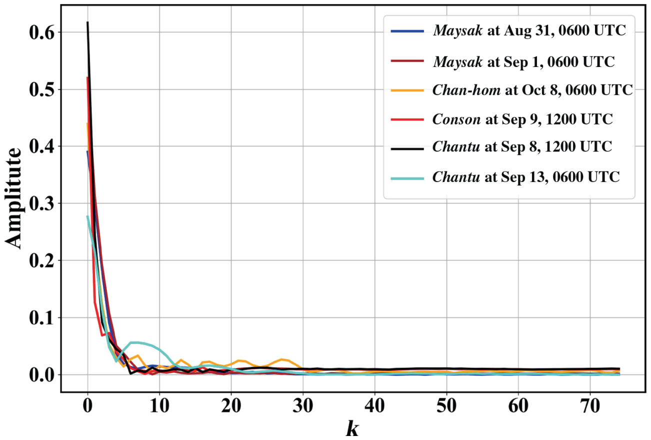

FIGURE 6 The spectrum corresponding to the sensitive area index of case nos. 1–6; the *x*-axis is the wave number, and the *y*-axis is the amplitude. [Colour figure can be viewed at wileyonlinelibrary.com]

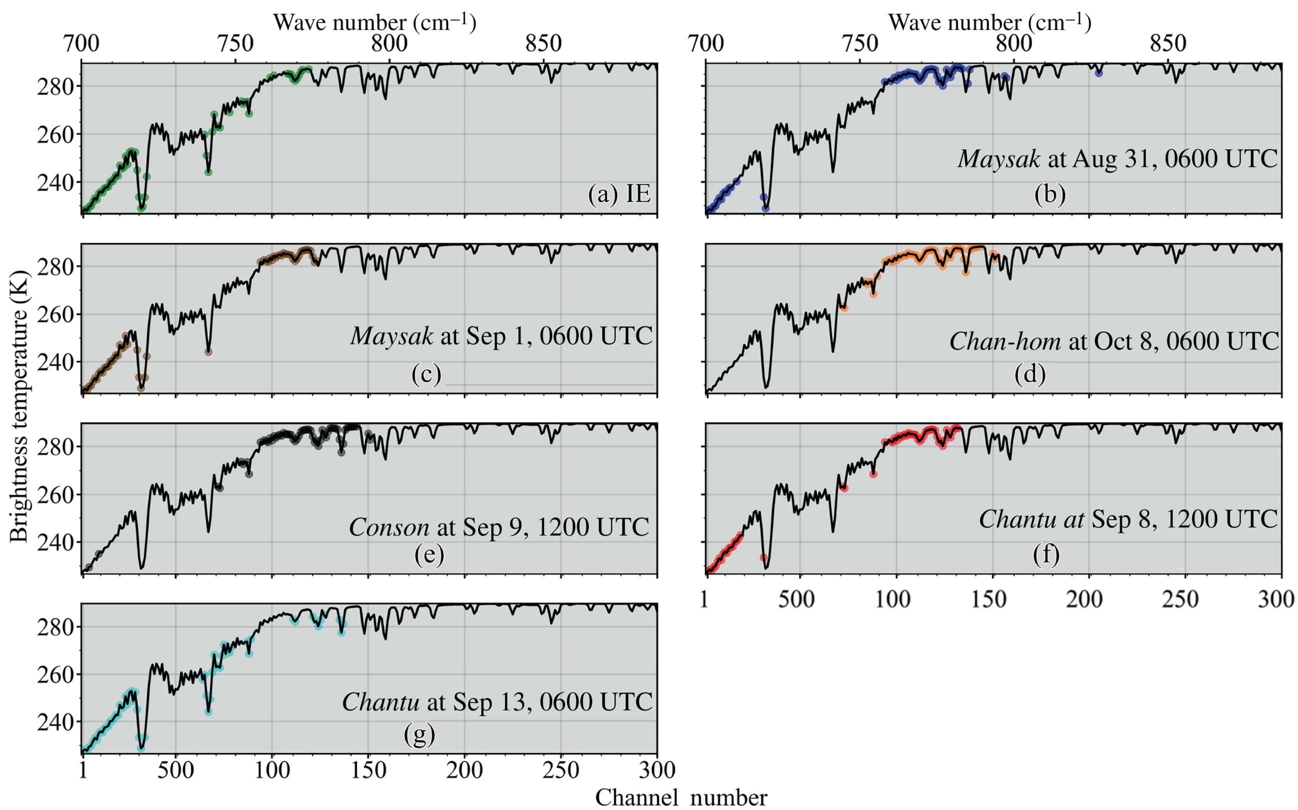

FIGURE 5 The brightness temperature values (black line). (a) The green dots represent the 60 channels selected by the information entropy (IE) method; (b)–(g) the 60 channels selected by the targeting satellite channel method for case nos. 1–6 respectively. The details of the channels in (a)–(g) are included in Supporting Information Tables S1–S7 respectively. [Colour figure can be viewed at wileyonlinelibrary.com]

Quarterly Journal of the Royal Meteorological Society

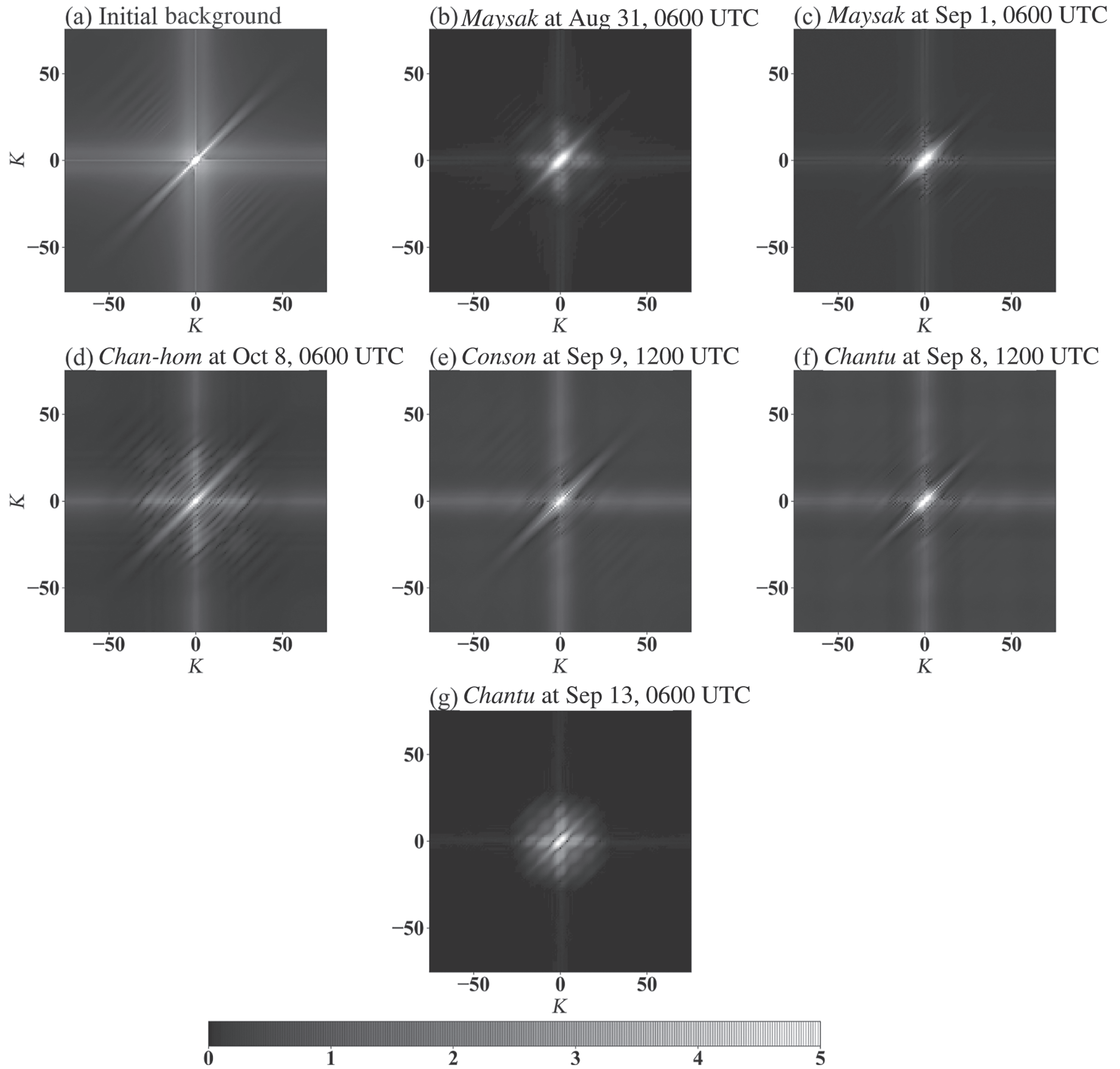

FIGURE 7 Spectra corresponding to (a) the initial background error covariance and (b)–(g) reconstructed background error covariance after weighting for case nos. 1–6; the *x*- and *y*-axes are the wave number.

and "small scale" specifically refer to the scale in the vertical direction, rather than the traditional concept of large scale. Corresponding to the Fourier transform of the background error covariance, we get that the initial background error is relatively uniformly distributed across large and small scales (Figure 7a). However, after being combined with the sensitive areas, which acts as a band-pass filter, the background error of all six cases (Figure 7b–g) primarily exhibits large-scale errors, whereas the small-scale error of *Chan-hom* is larger (Figure 7d) and the large-scale error is weaker than others corresponding to the amplitude of *Chan-hom* being small when the value of k is small (indicated by the orange line in Figure 6). When the wave number of *Chanthu* is 5–10, we observe that its amplitude is larger thanh the other cases (cyan line in Figure 6), which also corresponds to the background error covariance in Figure 7g. Similar results are available for the other cases (Figure 7b–f). The newly constructed background error covariance, incorporating the sensitive areas, effectively describes the specific initial error uncertainty in terms of size, position, and scale. As a result, the channels selected by the TSC method effectively capture the observation information from the sensitive areas, allowing for a reduction in the specific initial error.

4.2 | Fitting of background and analyses to observations

To assess the effectiveness of assimilation, it is crucial to compare the fitting of the background field before assimilation and the analysis after assimilation to the

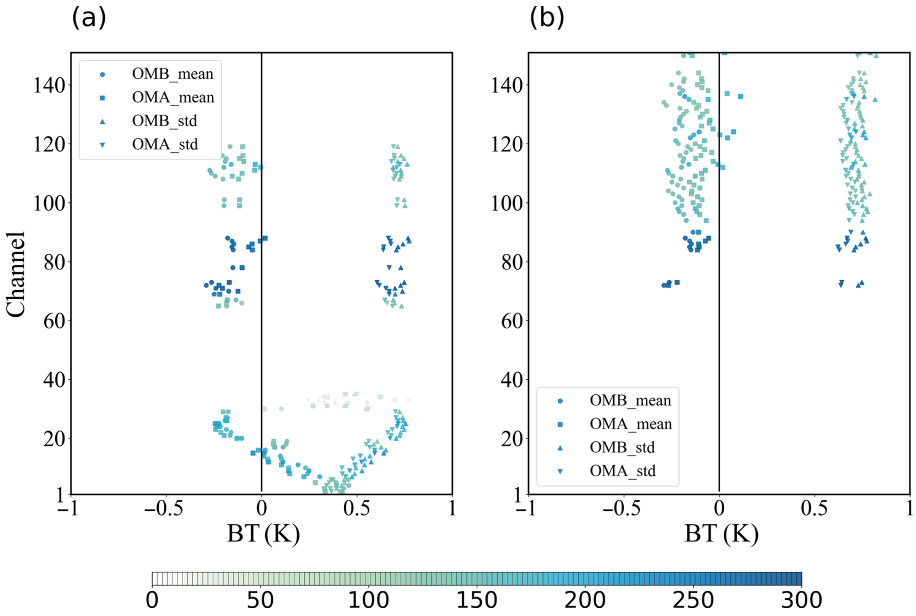

FIGURE 8 The mean and standard deviation of observation minus background (OMB) and observation minus analysis (OMA) (brightness temperature, BT) corresponding to different channels for *Chan-hom* corresponding to (a) the information entropy method (EXP_CTRL) and (b) the targeting satellite channe (EXP_SEN). Dots, squares, inverted triangles, and triangles correspond to the mean of OMB, the mean of OMA, the standard deviation (std) of OMB, and the std of OMA respectively. The color represents the number of corresponding channels that enter the assimilation system after quality control. [Colour figure can be viewed at wileyonlinelibrary.com]

GIIRS. Figure 8 shows the mean and standard deviation of observation minus background and observation minus analysis corresponding to the channels used in Typhoon *Chan-hom* within an assimilation time window. After the assimilation of the two groups of experiments EXP_CTRL (Figure 8a) and EXP_SEN (Figure 8b), the mean of the observation minus analysis is closer to zero and the standard deviation is smaller. These findings indicate that the analysis field, after assimilating the GIIRS brightness temperature, exhibits a better agreement with the independent observation results overall. The remaining cases yield similar outcomes, which are not shown here. In summary, the results shown in Figure 8 validate the effectiveness of assimilating the GIIRS brightness temperature in improving the accuracy of the initial analysis field.

4.3 | TC track forecasting

Forecasting the track of typhoons is a vital metric for assessing forecasting skills, and it is also a matter of widespread concern in society. Figure 9 shows the typhoon track of six typhoon cases under different experimental conditions, along with the CMA best-track dataset (represented by the black line in Figure 9). The results indicate that the forecasts without assimilating the GIIRS data (the green line of Figures 9 and 10) generally perform worse than EXP_CTR (the blue line of Figures 9 and 10), demonstrating the effectiveness of the GIIRS data. Additionally, in four out of the six cases, including typhoons *Chan-hom*, *Chanthu*, and *Conson* (Figure 10c–f), the typhoon track forecast of EXP_SEN (orange line in Figure 10) outperforms those of EXP_CTRL (blue line in Figure 10) throughout the forecast period. The improvement of the Typhoon *Chan-hom* track forecast reaches up to 87.25% at day 4. It is worth noting that for anomalous track forecasting of *Chanthu*(Figure 10f), EXP_SEN also outperforms EXP_SEN. For the two individual cases of *Maysak*(Figure 10a,b), the results of typhoon track forecasting of EXP_SEN and EXP_CTRL are similar in both cases. On average, EXP_SEN exhibits lower typhoon track forecast errors than EXP_CTRL does throughout the entire forecast period. At days 2–4 the mean track error is reduced by more than 35 km. Specifically, at day 3.5 the mean track error is reduced by 68.12 km (Figure 10g) and the track forecast is improved by 26.75% (Figure 10h). These results underscore the significant impact of the TSC method on enhancing the accuracy of typhoon track forecasting.

4.4 | Mechanisms

The difference between the typhoon track forecasts of EXP_SEN and EXP_CTRL is derived from the assimilation of observation data from different channels in the initial analysis. Consequently, it becomes crucial to examine the influence of various channels on the typhoon analysis field. Considering that the channels in vertical sensitive areas assimilated have a significant impact on the typhoon track forecast of Typhoon *Chan-hom*, we concentrate on analyzing this particular case to reveal how the channels assimilated in the sensitive areas affect the analysis field and forecast of Typhoon *Chan-hom*.

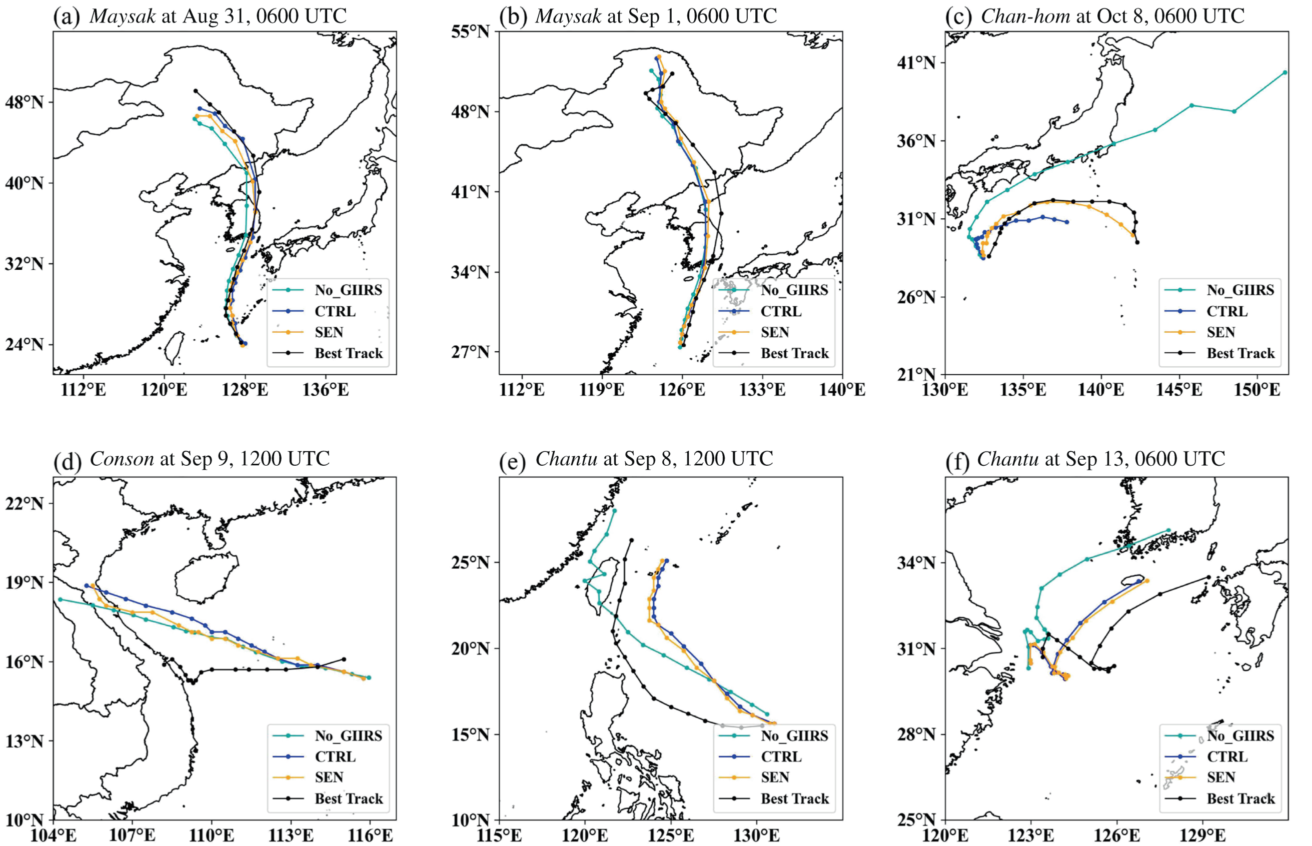

FIGURE 9 Forecasted typhoon track. The orange line is the forecast results of the EXP_SEN, the blue line is the forecast result of the EXP_CTRL, the green line is the forecast result of the No_GIIRS, and the black line comes from the China Meteorological Administration best-track dataset (Lu *et al.*, 2021; Ying *et al.*, 2014) (for the source of the dataset, please log in to https://tcdata.typhoon.org.cn). (a)–(f) Case nos. 1–6 respectively. [Colour figure can be viewed at wileyonlinelibrary.com]

It is well known that the motion of a typhoon is mainly controlled by steering flow in the middle and lower atmosphere. The steering flow is generally defined as the average wind vector in the typhoon environment within a certain radius in the middle troposphere. The steering flow is calculated by averaging the wind vectors with a typhoon as the center and a radius of 1,000 km (Ting-Chi *et al.*, 2014). It is worth noting that there is no direct wind observation assimilated in our study and most of the channels we choose are temperature channels, which mainly detect temperature variables. The difference between the two groups of experiments (EXP_CTRL and EXP_SEN) mainly arises from the difference of the initial temperature analysis field assimilating different channels. Therefore, it is crucial to study how the momentum field responds to the increment in the initial temperature field.

Figure 11 displays the steering flow at various levels under different lead times of EXP_CTRL (blue arrows) and EXP_SEN (orange arrows) for Typhoon *Chan-hom*, along with their difference in steering flow (red arrows). The initial steering flow of the two groups of experiments points to the northeast for almost the entire atmosphere (the left side of Figure 11), which is consistent with the subsequent northeastward movement of the typhoon track. Comparing EXP_SEN with EXP_CTRL, the initial steering flow has an increment of west wind in the middle and lower atmosphere (500–700 hPa), which is generally consistent with the eastward movement of the typhoon track in the EXP_SEN.

We further analyze how temperature differences resulting from the assimilation of different channels contribute to variations in the steering flow in the different atmospheric layers. In the following analysis, the variables (temperature, geopotential height, meridional wind, and zonal wind) represent the difference between EXP_SEN and EXP_CTRL, which still maintain a hydrostatic relationship and geostrophic wind relationship. In the typhoon-centered area with a radius of 1,000 km, the temperature field (Figure 12a) and the geopotential height field (Figure 12b) exhibit a relatively noticeable negative correlation below 500 hPa and a positive correlation above 500 hPa. This can be attributed to the expansion of gas caused by high temperatures in the lower layer, resulting in the upward movement of airflow, decreased air

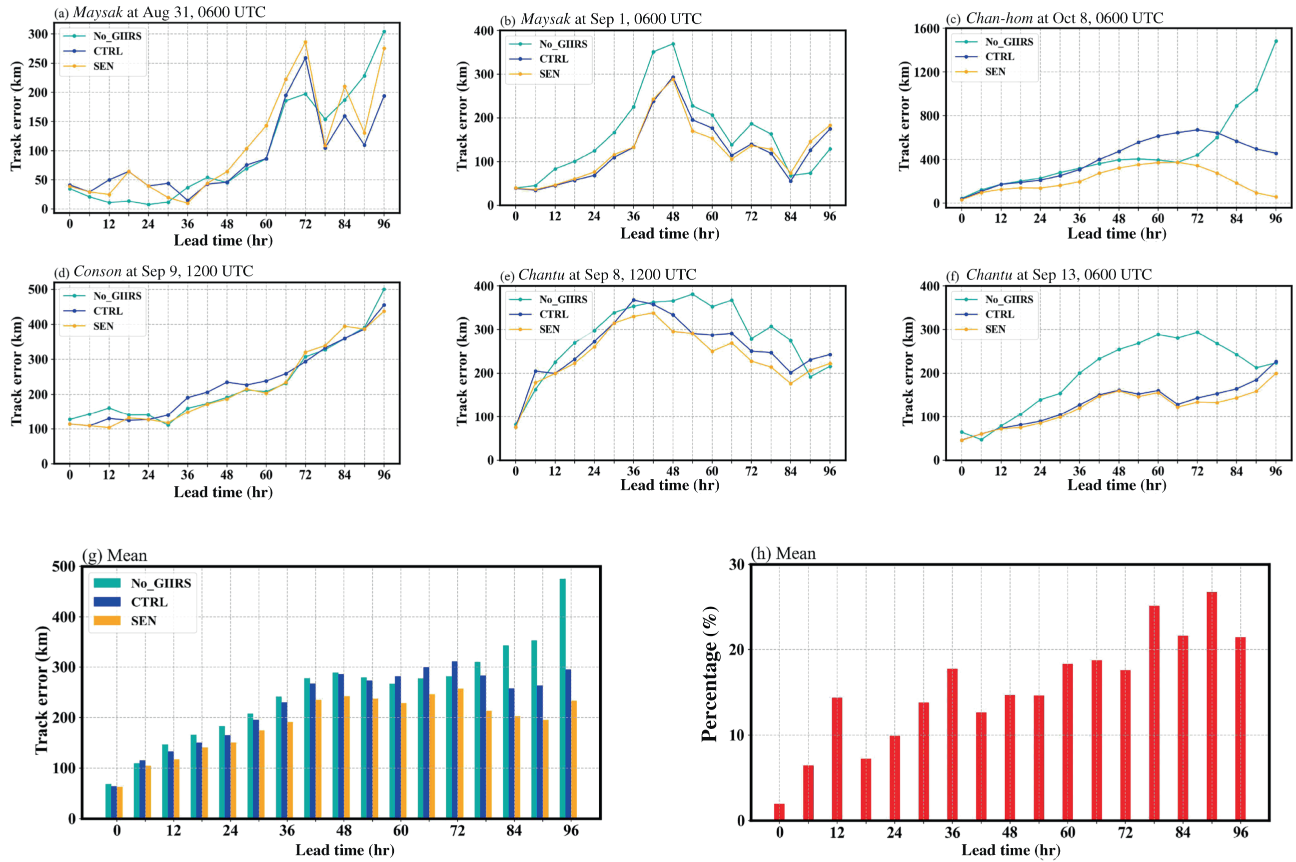

FIGURE 10 Typhoon track forecast errors (units: km) for EXP_SEN (orange), EXP_CTRL (blue), and No_GIIRS (green) verified against the China Meteorological Administration best-track for the six cases. (a)–(f) Case nos. 1–6 respectively; (g) the average track error for case nos. 1–6; (h) the improvement in track error for EXP_SEN compared with EXP_CTRL. [Colour figure can be viewed at wileyonlinelibrary.com]

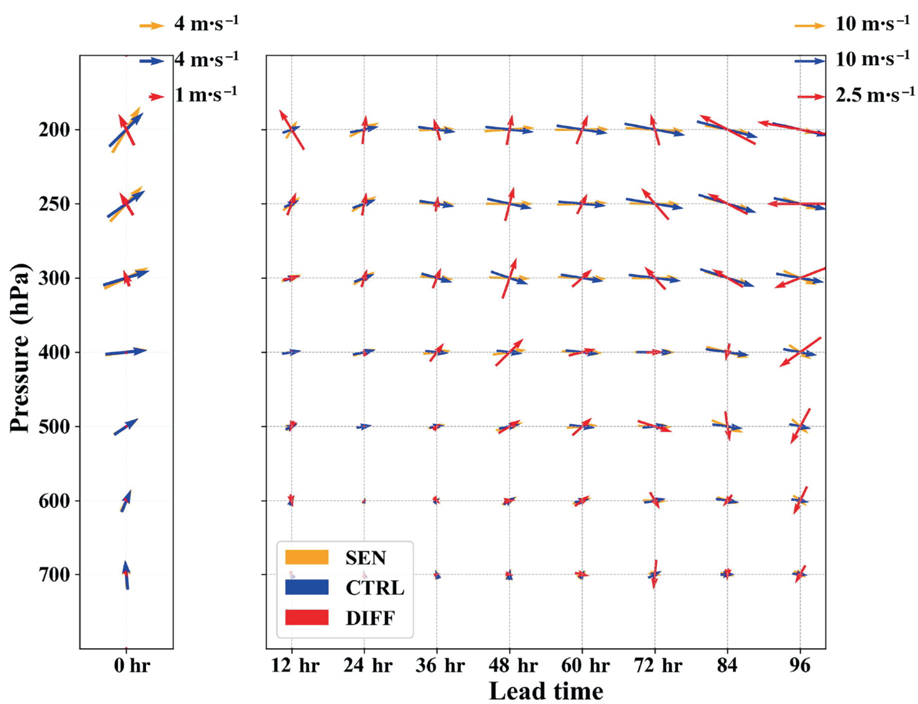

FIGURE 11 Steering flow of CTRL (blue) and SEN (orange) and their differences (red) at the (a) initial time and (b) forecast lead times for Typhoon *Chan-hom* initialized at 0600 UTC on October 8. [Colour figure can be viewed at wileyonlinelibrary.com]

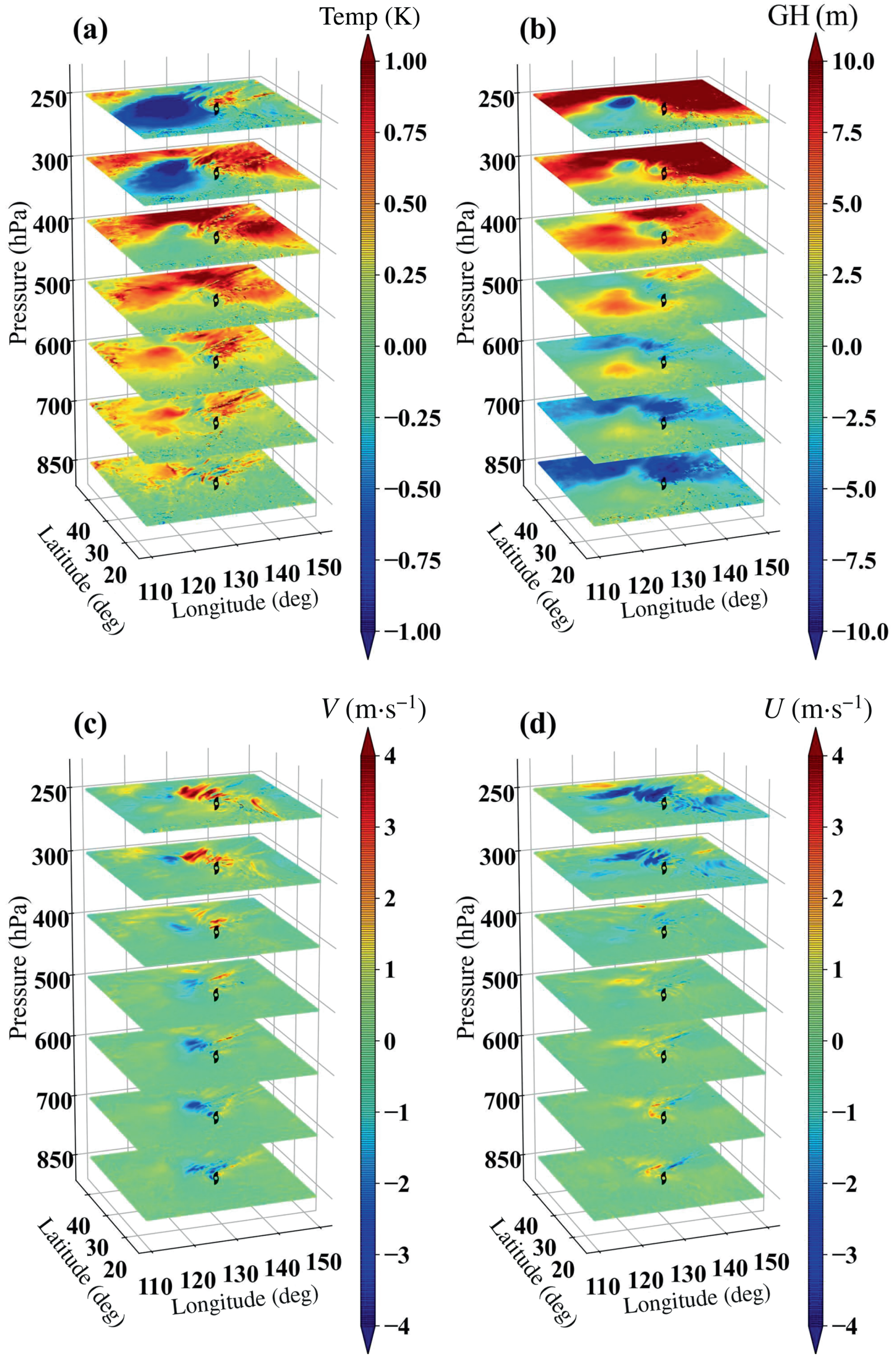

FIGURE 12 The three-dimensional structure of the difference of (a) temperature (T), (b) geopotential height (GH), (c) meridional wind (V), and (d) zonal wind (U) between EXP_SEN and EXP_CTRL which is centered on *Chan-hom* at 0600 UTC on October 8. The black typhoon sign represents the typhoon center. [Colour figure can be viewed at wileyonlinelibrary.com]

pressure, and subsequently decreased geopotential height. According to the hydrostatic relationship, the air pressure in warm air decreases more gradually with height compared with cold air, leading to an increase (decrease) in air pressure and an increase (decrease) in the geopotential height in the high- (low-)temperature area of the upper layer. The change in the geopotential height further leads to a change in the wind field. The meridional wind is negative (north wind) at the northwest side of the typhoon center below 500 hPa (Figure 12c), whereas the zonal wind is positive (west wind) at the northwest side of the typhoon center below 500 hPa (Figure 12d). These patterns are a result of the geopotential height modulating the wind field through the geostrophic wind relationship. The averaged wind vectors contribute to the differences in steering flow at 500–700 hPa, resulting in a southeastward flow. Under the constraints of the assimilation system, the aforementioned adjustments in other variable fields resulting from changes in the temperature field are accomplished. From the perspective of the vertical structure of the difference of steering flow (red arrows in Figure 11), we observe a transition from a northwestward wind in the lower troposphere to a southeastward wind in the upper troposphere. This indicates that the thermal wind is southeastward. Figure 12a shows that the northeast side of the typhoon is always high temperature, whereas the southwest side is low temperature, which conforms to the relationship of the thermal wind.

5 | CONCLUSIONS

This study aims to utilize the high spatiotemporal resolution observational characteristics of the GIIRS by dynamically selecting channels capable of reducing errors in vertical atmospheric layers with high sensitivity, thereby enhancing forecasting accuracy. Utilizing the high spectral resolution capabilities of GIIRS, we are able to perform adaptive observations of the sensitive areas across different vertical levels in the atmosphere. The proposed TSC selection method is developed based on the IE method, with a focus on observing the vertical sensitive areas. In this article, the CMA-GFS model and a four-dimensional variational data assimilating system were utilized to assimilate the GIIRS observation data to evaluate the validity of the TSC mrthod and the influence of the selected channels on the typhoon track forecasting (*Chan-hom*, *Maysak*, *Chanthu*, and *Conson*).

The primary findings reveal that the channels of the GIIRS selected through the TSC method predominantly capture the observational data of sensitive areas by reconstructing the background error covariance matrix. This reconstruction effectively captures the sizes, locations, and error scale characteristics inherent to the vertical sensitive areas for each typhoon. On average, assimilation channels selected by the TSC method demonstrated their effectiveness in improving track forecasts, with the mean track error of six cases reduced by more than 35 km from days 2 to 4. Specifically, at day 3.5, a reduction of 68.12 km in mean track error led to a 26.75% improvement in the track forecast. These findings highlight the considerable impact of the TSC method in enhancing the accuracy of typhoon track forecasting. In particular, for the case of *Chan-hom*, the forecasts of the typhoon track are notably improved when using channels selected by the TSC method.

A detailed analysis showed that the difference in temperature between EXP_SEN and EXP_CTRL influenced the initial momentum variables (i.e., the geopotential height and wind) under the constraints of the assimilation system, through the hydrostatic relationship. The initial steering flow of EXP_SEN of Typhoon *Chan-hom* is closer to the real situation, which contributed to the improved forecast skills of the TC track.

This research highlights the benefit of assimilating the channels from the GIIRS onboard the FY-4A satellite, selected by the TSC method, in improving the forecasts of the TC tracks. These positive impacts of assimilation indirectly show the effectiveness of targeted observations in the vertical atmosphere. So far, the observation information of the GIIRS with high vertical resolution has not been effectively utilized, and the TSC method can partially exploit its advantages. The GIIRS provides valuable observations to the structures of sensitive areas of TCs and the surrounding environment. Future investigations will explore how assimilating targeted observations of water vapor channels influences the moisture thermodynamic processes within TCs, potentially altering their development.

Although we made targeted observations of vertical sensitive areas by selecting different channels of the GIIRS, the observations in cloud and precipitation areas are excluded through cloud detection in data assimilation from the satellite. It is important to note that the main structure of a typhoon typically resides within these cloud and precipitation areas. Therefore, further investigation is needed to explore how to effectively assimilate satellite data in cloud and precipitation areas in order to utilize the full potential of the GIIRS for intensive observations in sensitive areas. In addition, the sensitive areas in this study are determined based on the LSV method. This method is mainly linear and cannot capture the nonlinear development of errors well. To address this, future research could incorporate the conditional nonlinear optimal perturbation method (Mu *et al.*, 2003), which is a nonlinear extension of LSV. Overall, these issues present opportunities for future research. Exploring methods to assimilate data in cloud and precipitation areas and incorporating nonlinear approaches such as the conditional nonlinear optimal perturbation method will contribute to a deeper understanding of the data assimilation from satellites.

ACKNOWLEDGEMENTS

This study was jointly supported by National Key Research and Development Program of China (2022YFC3004004), the International Partnership Program of Chinese Academy of Sciences (060GJHZ2022061MI), and National Natural Science Foundation of China (42075155). We appreciate the National Satellite Meteorological Center and Tropical Cyclone Data Center of China Meteorological Administration for their technical support in data.

DATA AVAILABILITY STATEMENT

The TC best-track dataset that support the findings of this study are openly available at https://tcdata.typhoon.org.cn. The FY-4A GIIRS data are available from the National Satellite Meteorological Center. Restrictions apply to the availability of the GIIRS data, which were used under licence for this study. GIIRS data are available with the permission of the National Satellite Meteorological Center.

ORCID

Yonghui Li https://orcid.org/0009-0003-0364-7600
Wei Han https://orcid.org/0000-0002-1966-446X
Wansuo Duan https://orcid.org/0000-0002-0122-2794

REFERENCES

Bergot, T. (1999) Adaptive observations during fastex: a systematic survey of upstream flights. *Quarterly Journal of the Royal Meteorological Society*, 125(561), 3271–3298.

Bergot, T., Hello, G., Joly, A. & Malardel, S. (1999) Adaptive observations: a feasibility study. *Monthly Weather Review*, 127(5), 743–765.

Buizza, R., Cardinali, C., Kelly, G. & Thepaut, J.N. (2007) The value of targeted observations—part ii: the value of observations taken in singular vectors based target areas. ecmwf research department technical memorandum n. 512, ecmwf, shinfield park. *Reading RG2-9AX, UK*.

Chen, J., Ma, Z., Li, Z., Shen, X., Yong, S., Chen, Q. et al. (2020) Vertical diffusion and cloud scheme coupling to the charney–phillips vertical grid in grapes global forecast system. *Quarterly Journal of the Royal Meteorological Society*, 146(730), 2191–2204.

Chun-Chieh, W., Chen, J.-H., Lin, P.-H. & Chou, K.-H. (2007) Targeted observations of tropical cyclone movement based on the adjoint-derived sensitivity steering vector. *Journal of the Atmospheric Sciences*, 64(7), 2611–2626.

Chun-Chieh, W., Lin, P.-H., Aberson, S., Yeh, T.-C., Huang, W.-P., Chou, K.-H. et al. (2005) Dropwindsonde observations for typhoon surveillance near the taiwan region (dotstar) an overview. *Bulletin of the American Meteorological Society*, 86(6), 787–790.

Collard, A.D. (2007) Selection of iasi channels for use in numerical weather prediction. *Quarterly Journal of the Royal Meteorological Society: A Journal of the Atmospheric Sciences, Applied Meteorology and Physical Oceanography*, 133(629), 1977–1991.

Coopmann, O., Guidard, V., Fourrié, N., Josse, B. & Marécal, V. (2020) Update of infrared atmospheric sounding interferometer (iasi) channel selection with correlated observation errors for numerical weather prediction (nwp). *Atmospheric Measurement Techniques*, 13(5), 2659–2680.

Dai, Y., Zeng, X., Dickinson, R.E., Baker, I., Bonan, G.B., Bosilovich, M.G. et al. (2003) The common land model. *Bulletin of the American Meteorological Society*, 84(8), 1013–1024.

Di, D., Li, J., Han, W., Bai, W., Chunqiang, W., Paul, W. et al. (2018) Enhancing the fast radiative transfer model for fengyun-4 giirs by using local training profiles. *Journal of Geophysical Research: Atmospheres*, 123(22), 12–583.

Feng, J., Qin, X., Chunqiang, W., Zhang, P., Yang, L., Shen, X. et al. (2022) Improving typhoon predictions by assimilating the retrieval of atmospheric temperature profiles from the fengyun-4a's geostationary interferometric infrared sounder (giirs). *Atmospheric Research*, 280, 106391.

Froude, L.S.R., Bengtsson, L. & Hodges, K.I. (2007) The predictability of extratropical storm tracks and the sensitivity of their prediction to the observing system. *Monthly Weather Review*, 135(2), 315–333.

Joly, A., Jorgensen, D., Shapiro, M.A., Thorpe, A., Bessemoulin, P., Browning, K.A. et al. (1997) The fronts and atlantic storm-track experiment (fastex): scientific objectives and experimental design. *Bulletin of the American Meteorological Society*, 78(9), 1917–1940.

Kim, Y.-J. & Arakawa, A. (1995) Improvement of orographic gravity wave parameterization using a mesoscale gravity wave model. *Journal of Atmospheric Sciences*, 52(11), 1875–1902.

Langland, R.H., Toth, Z., Ret Gelaro, I., Szunyogh, M.A.S., Majumdar, S.J., Morss, R.E. et al. (1999) The north pacific experiment (norpex-98): targeted observations for improved north american weather forecasts. *Bulletin of the American Meteorological Society*, 80(7), 1363–1384.

Lott, F. & Miller, M.J. (1997) A new subgrid-scale orographic drag parametrization: its formulation and testing. *Quarterly Journal of the Royal Meteorological Society*, 123(537), 101–127.

Lu, X.Q., Yu, H., Ying, M., Zhao, B.K., Zhang, S., Lin, L.M. et al. (2021) Western North Pacific tropical cyclone database created by the China Meteorological Administration. *Advances in Atmospheric Sciences*, 38(4), 690–699.

Ma, Z., Liu, Q., Zhao, C., Shen, X., Wang, Y., Jiang, J.H. et al. (2018) Application and evaluation of an explicit prognostic cloud-cover scheme in grapes global forecast system. *Journal of Advances in Modeling Earth Systems*, 10(3), 652–667.

Majumdar, S.J., Bishop, C.H., Buizza, R. & Gelaro, R. (2002) A comparison of ensemble-transform kalman-filter targeting guidance with ecmwf and nrl total-energy singular-vector guidance. *Quarterly Journal of the Royal Meteorological Society: A Journal of the Atmospheric Sciences, Applied Meteorology and Physical Oceanography*, 128(585), 2527–2549.

Morcrette, J.J., Barker, H.W., Cole, J.N.S., Iacono, M.J. & Pincus, R. (2008) Impact of a new radiation package, mcrad, in the ecmwf integrated forecasting system. *Monthly Weather Review*, 136(12), 4773–4798.

Mu, M., Duan, W.S. & Wang, B. (2003) Conditional nonlinear optimal perturbation and its applications. *Nonlinear Processes in Geophysics*, 10(6), 493–501.

Palmer, T.N., Gelaro, R., Barkmeijer, J. & Buizza, R. (1998) Singular vectors, metrics, and adaptive observations. *Journal of the Atmospheric Sciences*, 55(4), 633–653.

Parrish, D.F. & Derber, J.C. (1992) The national meteorological center's spectral statistical-interpolation analysis system. *Monthly Weather Review*, 120(8), 1747–1763.

Paul Menzel, W., Schmit, T.J., Zhang, P. & Li, J. (2018) Satellite-based atmospheric infrared sounder development and applications. *Bulletin of the American Meteorological Society*, 99(3), 583–603.

Pincus, R., Barker, H.W. & Morcrette, J.-J. (2003) A fast, flexible, approximate technique for computing radiative transfer in inhomogeneous cloud fields. *Journal of Geophysical Research: Atmospheres*, 108(D13), 4376.

Qin, X., Duan, W., Chan, P.-W., Chen, B. & Huang, K.-N. (2023) Effects of dropsonde data in field campaigns on forecasts of tropical cyclones over the western north pacific in 2020 and the role of cnop sensitivity. *Advances in Atmospheric Sciences*, 40(5), 791–803.

Qin, X. & Mu, M. (2014) Can adaptive observations improve tropical cyclone intensity forecasts? *Advances in Atmospheric Sciences*, 31, 252–262.

Rabier, F., Fourrié, N., Chafäi, D. & Prunet, P. (2002) Channel selection methods for infrared atmospheric sounding interferometer radiances. *Quarterly Journal of the Royal Meteorological Society: A Journal of the Atmospheric Sciences, Applied Meteorology and Physical Oceanography*, 128(581), 1011–1027.

Rabier, F., Klinker, E., Courtier, P. & Hollingsworth, A. (1996) Sensitivity of forecast errors to initial conditions. *Quarterly Journal of the Royal Meteorological Society*, 122(529), 121–150.

Reynolds, C.A., Webster, P.J. & Kalnay, E. (1994) Random error growth in nmc's global forecasts. *Monthly Weather Review*, 122(6), 1281–1305.

Rodgers, C.D. (1998) Information content and optimization of high-spectral-resolution measurements. *Advances in Space Research*, 21(3), 361-367.

Shannon, C.E. (1949) Communication in the presence of noise. *Proceedings of the IRE*, 37(1), 10–21.

Simmons, A.J. (1995) High-performance computing requirements for medium-range weather forecasting. *ECMWF Newslett*, 69, 8–13.

Simmons, A.J. & Hollingsworth, A. (2002) Some aspects of the improvement in skill of numerical weather prediction. *Quarterly Journal of the Royal Meteorological Society: A Journal of the Atmospheric Sciences, Applied Meteorology and Physical Oceanography*, 128(580), 647–677.

Snyder, C. (1996) Summary of an informal workshop on adaptive observations and fastex. *Bulletin of the American Meteorological Society*, 77(5), 953–961.

Ting-Chi, W., Liu, H., Majumdar, S.J., Velden, C.S. & Anderson, J.L. (2014) Influence of assimilating satellite-derived atmospheric motion vector observations on numerical analyses and forecasts of tropical cyclone track and intensity. *Monthly Weather Review*, 142(1), 49–71.

Torn, R.D. (2014) The impact of targeted dropwindsonde observations on tropical cyclone intensity forecasts of four weak systems during predict. *Monthly Weather Review*, 142(8), 2860–2878.

Vigh, J.L. & Schubert, W.H. (2009) Rapid development of the tropical cyclone warm core. *Journal of the Atmospheric Sciences*, 66(11), 3335–3350.

Wang, J., Wang, B., Liu, J., Liu, Y., Chen, J. & Huo, Z. (2020) Application and characteristic analysis of the moist singular vector in grapes-geps. *Advances in Atmospheric Sciences*, 37, 1164–1178.

Xiaoqin, L., Hui, Y., Ying, M., Zhao, B., Zhang, S., Lin, L. et al. (2021) Western north pacific tropical cyclone database created by the china meteorological administration. *Advances in Atmospheric Sciences*, 38, 690–699.

Yamaguchi, M. & Majumdar, S.J. (2010) Using tigge data to diagnose initial perturbations and their growth for tropical cyclone ensemble forecasts. *Monthly Weather Review*, 138(9), 3634–3655.

Yamaguchi, M., Sakai, R., Kyoda, M., Komori, T. & Kadowaki, T. (2009) Typhoon ensemble prediction system developed at the japan meteorological agency. *Monthly Weather Review*, 137(8), 2592–2604.

Yang, J., Zhang, Z., Wei, C., Feng, L. & Guo, Q. (2017) Introducing the new generation of chinese geostationary weather satellites, fengyun-4. *Bulletin of the American Meteorological Society*, 98(8), 1637–1658.

Yin, R., Han, W., Gao, Z. & Li, J. (2021) Impact of high temporal resolution fy-4a geostationary interferometric infrared sounder (giirs) radiance measurements on typhoon forecasts: Maria (2018) case with grapes global 4d-var assimilation system. *Geophysical Research Letters*, 48(15), e2021GL093672.

Yin, R.Y., Han, W., Gao, Z.Q. & Wang, G. (2019) A study on longwave infrared channel selection based on estimates of background errors and observation errors in the detection area of fy-4a. *Acta Meteorologica Sinica*, 77(5), 898–910.

Ying, M., Zhang, W., Hui, Y., Xiaoqin, L., Feng, J., Fan, Y. et al. (2014) An overview of the china meteorological administration tropical cyclone database. *Journal of Atmospheric and Oceanic Technology*, 31(2), 287–301.

Zhang, D.-L. & Chen, H. (2012) Importance of the upper-level warm core in the rapid intensification of a tropical cyclone. *Geophysical Research Letters*, 39(2), L02806. https://agupubs.onlinelibrary.wiley.com/doi/epdf/10.1029/2002JD003322. [Accessed 24th May 2024].

Zhang, L., Liu, Y., Liu, Y., Gong, J., Huijuan, L., Jin, Z. et al. (2019) The operational global four-dimensional variational data assimilation system at the china meteorological administration. *Quarterly Journal of the Royal Meteorological Society*, 145(722), 1882–1896.

Zhou, F. & Mu, M. (2011a) The impact of verification area design on tropical cyclone targeted observations based on the cnop method. *Advances in Atmospheric Sciences*, 28, 997–1010.

Zhou, F. & Mu, M. (2011b) The impact of verification area design on tropical cyclone targeted observations based on the cnop method. *Advances in Atmospheric Sciences*, 28, 997–1010.

Zhou, F. & Mu, M. (2012a) The time and regime dependencies of sensitive areas for tropical cyclone prediction using the cnop method. *Advances in Atmospheric Sciences*, 29, 705–716.

Zhou, F. & Mu, M. (2012b) The impact of horizontal resolution on the cnop and on its identified sensitive areas for tropical cyclone predictions. *Advances in Atmospheric Sciences*, 29, 36–46.

SUPPORTING INFORMATION

Additional supporting information can be found online in the Supporting Information section at the end of this article.

How to cite this article: Li, Y., Han, W. & Duan, W. (2024) Dynamic channel selection based on vertical sensitivities for the assimilation of FY-4A geostationary interferometric infrared sounder targeted observations. *Quarterly Journal of the Royal Meteorological Society*, 1–17. Available from: https://doi.org/10.1002/qj.4760

APPENDIX

Vertical sensitive areas

In previous studies, the horizontal sensitive areas were defined by vertically integrating the total dry energy (Buizza *et al.*, 2007; Zhou & Mu, 2012a, 2012b). This integration was performed using the following equation:

$$f(i,j) = \int_0^1 E_{\mathrm{d}}(i,j,\sigma)\, d\sigma, \tag{A.1}$$

where $E_{\mathrm{d}}(i,j,\sigma)$ is the dry total energy of the sensitive areas at the grid point (i,j,σ), which also can apply to wet total energy (Qin *et al.*, 2023). The horizontal grid points where the value $f(i,j)$ is larger than a certain value c are defined as the horizontal sensitive areas. Similar to the horizontal sensitive areas, the vertical sensitive areas are defined thus:

$$k(\sigma) = \int_D E_{\mathrm{w}}(i, j, \sigma)\, dD, \tag{A.2}$$

where D is the full domain, but $E_{\mathrm{w}}(i, j, \sigma)$ is the wet total energy of the sensitive areas, which can interpret wet processes that are important to typhoon structure. Unlike the horizontal direction, there is no need to define a threshold c for the vertical sensitive areas. Owing to its relatively small scale, we consider the structure of the vertical sensitive areas in the entire vertical direction.

The accuracy of the temperature field directly affects the structure of the warm core of the typhoon, which in turn affects the track and intensity of typhoons (Vigh & Schubert, 2009; Zhang & Chen, 2012). In order to better describe the vertical structure of temperature and make more efficient use of long-wave channels (1–300, 700–887.5 cm^{-1}) of the GIIRS, which are mostly temperature channels, we use thermal energy to define the vertical sensitive areas of thermal energy. The formula is as follows:

$$k(\sigma)' = \int_D \frac{c_p}{T_{\mathrm{r}}} T'^2\, dD, \tag{A.3}$$

where $k(\sigma)'$ only integrates thermal energy in the horizontal direction, which mainly depicts the vertical structure of the temperature error. In order to later weight the background error covariance, the sensitive area index SA is defined here; that is, the energy is standardized, and the formula is as follows:

$$\mathrm{SA} = \frac{k(\sigma)'}{\max(k(\sigma)')}, \tag{A.4}$$

LSV

This section provides a brief introduction to the LSV method, as detailed in Palmer *et al.* (1998).

A nonlinear model can be described as

$$\frac{\partial X}{\partial t} + F(X) = 0, \tag{A.5}$$

where F is a nonlinear partial differential operator. The initial conditions of the model can be described as

$$X|_{t=0} = X_0. \tag{A.6}$$

The state of the atmosphere at time t is X_t, which is the solution of Equation (A.5), which can be expressed as

$$X_t = M(X_0), \tag{A.7}$$

where M is the nonlinear propagator. Here, δX_0 is defined as the initial perturbation, δX_t is defined as the evolution of the initial perturbation, and $\delta X_t'$ is defined as the linear evolution of the initial perturbation at time t. When δX_0 is sufficiently small and the integration time interval is moderate, there is

$$\delta X_t' = L(\delta X_0) \approx M(X_0 + \delta X_0) - M(X_0) = \delta X_t, \tag{A.8}$$

where L is the forward tangent propagator.The singular values σ of L satisfy the following:

$$\sigma^2 = \frac{[L(\delta X_0)]^{\mathrm{T}} G_2 [L(\delta X_0)]}{[\delta X_0]^{\mathrm{T}} G_1 [\delta X_0]}, \tag{A.9}$$

where G_2 and G_1 are the norms. If v is the eigenvector corresponding to σ^2, then

$$\sigma^2 v = (G_1)^{-1}(L^T G_2 L) v, \tag{A.10}$$

where superscript -1 denotes the inverse of the matrix. In this article, $G_2 = G_1$, which represents the metric of wet total energy; in a continuous expression it can be expressed as

$$[\delta X_0]^{\mathrm{T}} G_1 [\delta X_0] = \frac{1}{D} \int_0^1 \int_D \left[u'^2 + v'^2 + \frac{c_p}{T_{\mathrm{r}}} T'^2 + R_{\mathrm{a}} T_{\mathrm{r}} \left(\frac{p_{\mathrm{s}}'}{p_{\mathrm{r}}} \right)^2 + \frac{L^2}{c_p T_{\mathrm{r}}} q'^2 \right] dD\, d\sigma, \tag{A.11}$$

where c_p and R_{a} are the specific heat at constant pressure and the gas constant of air respectively (with numerical values of 1,005.7 $\mathrm{J{\cdot}kg^{-1}\ {\cdot}K^{-1}}$ and 287.04 $\mathrm{J{\cdot}kg^{-1}\ {\cdot}K^{-1}}$ respectively). The reference parameters are as follows: $T_{\mathrm{r}} = 270$ K, $p_{\mathrm{r}} = 1{,}000$ hPa, $L = 2.5104 \times 10^6\ \mathrm{J{\cdot}kg^{-1}}$. Here, u', v', T', p_{s}', and q', which are components of the state vector, are the perturbed zonal and meridional wind components, temperature, surface pressure, and moisture respectively. The integration extends over the full domain D and the vertical direction σ. The δX_0^* is defined as a LSV if the eigenvalue σ^2 corresponding to δX_0^* is the largest.